PHYSICAL REVIEW E **103**, 063103 (2021)

Bubble cascade may form not only in stout beers

Tomoaki Watamura [*] and Kazuyasu Sugiyama
Graduate School of Engineering Science, Osaka University, 1-3, Mchikaneyama, Toyonaka, Osaka 560-8531, Japan
and RIKEN Center for Advanced Photonics, RIKEN, 2-1, Hirosawa, Wako, Saitama 351-0198, Japan

Yuko Yotsumoto, Mihoko Suzuki, and Hideyuki Wakabayashi
Institute for Future Beverages, Kirin Holdings Co. Ltd., 1-17-1, Namamugi, Tsurumi-ku, Yokohama, Kanagawa 230-8628, Japan

(Received 25 February 2021; revised 11 May 2021; accepted 18 May 2021; published 7 June 2021)

In a glass of stout beer, a very large number of small dispersed bubbles form a texture motion of a bubble swarm moving downwards. Such a cascading motion is caused by a gravity-driven hydrodynamic instability and depends on the interbubble distance. To estimate these two corresponding indicators, an experimentally measured velocity profile is required and, thus, is obtained *a posteriori*. However, it is unknown why the bubble cascade is observed only in stout beer with nitrogen, such as Guinness beer. To address this question via *a priori* estimation, here, we develop a mathematical continuum model of film flow in bubbly liquid, uncovering the essential dynamics among many physical processes occurring simultaneously in a glass. To validate the proposed model, we perform a numerical simulation of the distribution of massless Lagrangian particles in an inclined container. We investigate the effects of particle concentration, inclination angle, particle diameter, and container size on the cascading film flow. The results reveal that the motion and waviness of clear-fluid film can be successfully estimated *a priori* to experiments or simulations. Moreover, it is found that the continuum behavior of particles in the film flow is analogous to the continuum description of rarefied gas dynamics. These findings explain how the cascading bubbles in a pint glass of stout beer satisfy the continuum assumption and suggest a general condition for the onset of the cascade, for instance, a 200-l drum for carbonated water.

DOI: 10.1103/PhysRevE.103.063103

I. INTRODUCTION

A "continuum" is a matter comprising a sufficiently large number of grains, particles, or molecules, e.g., a cubic millimeter of atmosphere consists of 2.7×10^{16} molecules under standard conditions [1]. The Knudsen number $\mathrm{Kn}(=\lambda/\mathcal{L})$, which is the ratio of the mean free path λ to the characteristic length $\mathcal{L}$, is the conventional indicator of the degree of rarefaction of a gas and becomes $\mathrm{Kn} \ll 1$ for air with $\lambda \sim 50$ nm and $\mathcal{L} \sim 50\ \mu$m (i.e., the diameter of a typical human hair). Therefore, people walking on the Earth perceive air as a continuum [1,2]. In nature, loosely packed particles often flow like a liquid, e.g., sand around a swimming sandfish lizard [3], snow and ice particles in avalanches [4], debris in pyroclastic flows [5], and granular materials in fluidized beds [6,7]. Such a collective particle motion can be successfully explained in terms of the gravity-driven Rayleigh-Taylor instability by applying an approximation of a particle mixture to a continuum medium.

Although dispersed, i.e., noncontacting with each other, particles seemingly behave individually, fluidlike behaviors of a fingering pattern are occasionally observed in a naturally occurring stratified suspension, such as micro-organisms in aqueous environments [8] and volcanic ash in the atmosphere [9] or sea [10]. On a pub table, such a continuum approximation can be also observed in a glass of Guinness beer [11,12] in which bubbles with a mean diameter of $\sim 50\ \mu$m move downwards and form a wavy-structured texture. A movie is also available in the Supplemental Material [13]. This phenomenon is driven by two sets of dynamics. First, the rising motion of individual bubbles creates a clear-fluid (bubble-free) film near the inclined glass wall. The dense clear-fluid film falls, whereas the bubble-rich bulk rises; this is known as the Boycott effect [14]. Accordingly, we can observe the descending bubbles entrained into the downward flow. Second, the texture formation is caused by a roll wave, i.e., by the hydrodynamic instability of the falling liquid film [12,15]. However, unlike other beers, champagne, or carbonated water containing sub-millimeter-sized bubbles [16,17], the bubbles in Guinness beer behave collectively. The collective behavior of bubbles in a drink is not fully predicted yet.

In a glass of stout beer with nitrogen, we observe complex fluid motion owing to many physical processes that occur simultaneously: nucleation and expansion of bubbles [16], modification of the rise motion [18], bubble-driven convection, etc. Successful analysis of the texture formation has only recently been enabled by overcoming the difficulty in optical velocimetry of dense bubbly liquid [12,19]. The experimentally measured velocities have clarified two mechanisms relevant to causing the formation, namely, the roll-wave instability [12] and the sharpness of density profile [19], but these two corresponding indicators can be estimated *a posteriori*. For this reason, to comprehend the individual or collective motion of bubbles in drinks, we must conduct an experiment on pouring a drink in a glass. For *a priori* estimation of the

---

[*] tomoaki.watamura@me.es.osaka-u.ac.jp

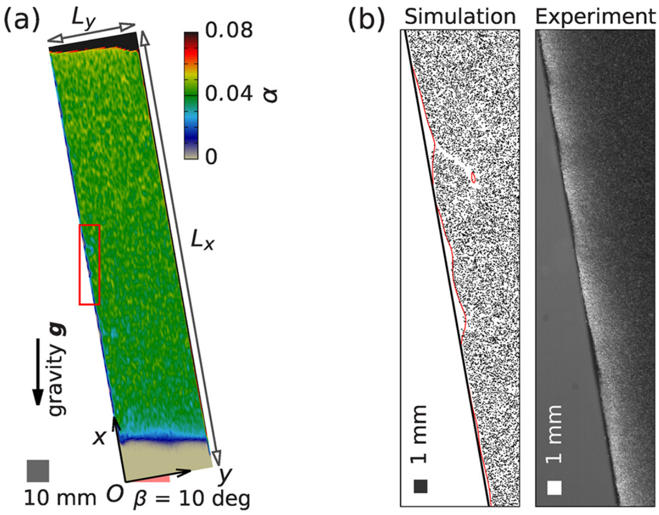

FIG. 1. (a) Configuration and snapshot of particle concentration distribution. Size of the container: $L_x \times L_y \times L_z = 200 \times 40 \times 0.1$ mm^3; inclination angle of the container: $\beta = 10^\circ$; diameter of particles: $a = 50 \pm 2$ μm; bulk particle concentration: $\langle\alpha\rangle = 0.04$; density of the liquid: $\rho = 1000$ kg/m^3; viscosity of the liquid: $\mu = 2.0 \times 10^{-3}$ Pa · s. (b) Comparison of the distribution of simulated particles (left) and Guinness beer bubbles (right) at the midpoint $x = L_x/2$. The corresponding zoomed-in area is marked with a red rectangle in (a). The red thin line indicates the interface at a particle concentration of $0.5 \times \langle\alpha\rangle$.

texture formation, developing the mathematical description of a stratified fluid motion still remains a key challenge that has motivated many studies over the past decade [11,20,21]. Herein, we address this issue by developing a mathematical continuum model of film flow that accounts for the relative velocity of particles with respect to the surrounding liquid phase. The model presented herein algebraically describes the motion of a falling clear-fluid film and successfully predicts the critical condition of continuum approximation and the onset of roll-wave instability without requiring experimental and numerical simulation results.

II. METHOD

A. Numerical simulation

As understanding of two-dimensional (2D) fluid motion is essential in modeling the dynamics of flow instability in thin liquid films [22], we numerically studied the behavior of bubbles in a spontaneously stratified suspension in an inclined container using the locally phase-averaged four-way coupling model applying the Eulerian-Lagrangian approach [23] with a discrete element method [24,25] as shown in Fig. 1(a). For this paper, we use the in-house code. The particles are assumed to distribute uniformly in the analysis domain and be stationary at $t = 0$ s. They are tracked as Lagrangian particles via a model equation in which the force of added mass, drag, gravity, and particle collision are taken into account. We focus on spherical nondeformable particles with diameter a, which are smaller than the fluid scale at low particle Reynolds number $\mathrm{Re}(=\rho a|\boldsymbol{v} - \boldsymbol{u}|/\mu) < 1$, where ρ is the fluid density, μ is the dynamic viscosity of the fluid, $\boldsymbol{u}$ is the fluid velocity, and $\boldsymbol{v}$ is the particle velocity. We use the Stokes drag coefficient $C_D = 24\,\mathrm{Re}^{-1}$ [2]. The equation of motion of the ith particle is given by Newton's second law of motion as follows [23,26]:

$$\frac{d\boldsymbol{y}_i}{dt} = \boldsymbol{v}_i, \tag{1}$$

$$\frac{d\boldsymbol{v}_i}{dt} = 3\left.\frac{D\boldsymbol{u}}{Dt}\right|_{\boldsymbol{y}_i} + \frac{1}{\tau_\mathrm{p}}(\boldsymbol{v}_i - \boldsymbol{u}|_{\boldsymbol{y}_i}) - 2\boldsymbol{g} + \frac{2\boldsymbol{F}_i^\mathrm{col}}{\rho V_\mathrm{p}}, \tag{2}$$

$$\tau_\mathrm{p} = \frac{\rho a^2}{36\mu}. \tag{3}$$

Here, $\boldsymbol{y}$ is the instantaneous position of the particle $V_\mathrm{p}(=\pi a^3/6)$ is the particle volume, $D/Dt(\equiv \partial/\partial t + \boldsymbol{u}\cdot\nabla)$ is the material derivative, $\boldsymbol{g}$ is the acceleration of gravity, and $\boldsymbol{F}_i^\mathrm{col}$ is the total contact force acting on the ith particle from the other particles and walls. The motion of the fluid phase is described using the Navier-Stokes equation for an incompressible flow as follows:

$$\frac{\partial\alpha}{\partial t} + \nabla\cdot(\alpha\boldsymbol{u}) = 0, \tag{4}$$

$$\frac{D\boldsymbol{u}}{Dt} = -\frac{\nabla p}{\rho} + \frac{1}{\rho}\nabla\cdot[\mu(\nabla\boldsymbol{u} + \nabla\boldsymbol{u}^T)] + \boldsymbol{g} + \boldsymbol{f}_\mathrm{p}, \tag{5}$$

$$\boldsymbol{f}_\mathrm{p} = \sum_{i\,\mathrm{in}\,\mathcal{V}}\left[\left(\frac{D\boldsymbol{u}}{Dt} - \boldsymbol{g}\right)\frac{V_\mathrm{p}}{\mathcal{V}} + \frac{\boldsymbol{F}_i^\mathrm{col}}{\rho\mathcal{V}}\right]\delta(\boldsymbol{x} - \boldsymbol{y}_i), \tag{6}$$

where p is the pressure, $\boldsymbol{f}_\mathrm{p}$ is the feedback force from the particle to the fluid phase, δ is the smoothed δ function [27], which considers all lattice nodes up to the nearest 3×3 points, and $\mathcal{V}$ is the control volume of the simulation. At the wall surface, we impose the Dirichlet no-slip boundary condition for velocity and the Neumann boundary condition for the pressure and particle concentration.

For the most simplified model for a simulation, we neglect the increase in the bulk viscosity of suspension arising from the presence of dispersed bodies, i.e., the effective viscosity [28], and the reduction in the rise velocity of dispersed bodies in suspensions, i.e., the hindered velocity [29]. Increasing the viscosity reduces the descending film velocity, whereas decreasing the rise velocity of the bubbles reduces the clear-fluid layer thickness; the modification of these fluid properties stabilizes the flow. In this paper, we set $\langle\alpha\rangle = 0.04$ at the maximum, and, therefore, the modifications of viscosity ($\sim 5/2\alpha$ [28]) and rise velocity ($\sim -1.76\alpha^{1/3}$ or $\sim -3/\sqrt{2}\alpha^{1/2}$ [29]) have only a minor effect on the fluid motion scaling and can be neglected. This simplification allows us to compare the flow state obtained from the simulation and the continuum flow model. The unsteady fluid motion is visualized using the locally averaged particle concentration via the 3×3 points smoothed δ function [27] [Fig. 1(a)] and the individual particle positions [Fig. 1(b)]. In these visualizations, a clear-fluid (particle-free) film forms above the inclined wall and then flows downwards (see also the Supplemental Material [13] for a video).

B. Experiment

We conduct a series of experiments on transparent "pseudo Guinness beer," a particle suspension comprising tap water

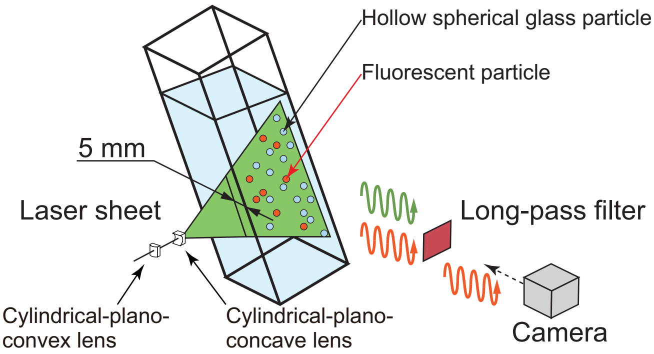

FIG. 2. Experimental setup for measuring liquid phase velocity via PIV-LIF using laser and high-speed video camera.

and hollow spherical glass particles with a mean diameter of 47 μm and a density of 140 kg/m^3 [12]. The velocity of the liquid phase was obtained via particle image velocimetry (PIV) [30]. Figure 2 shows the experimental setup used to conduct PIV, comprising a laser and a high-speed video camera. To distinguish tracer particles within the suspension, we applied the laser-induced-fluorescence (LIF) technique to PIV [31]. Fluorescent tracer particles with a diameter of 15 μm were seeded at 0.03 vol. % into the particle suspension. The laser light reflected from the particle interface is blocked by an optical long-pass filter placed in front of the high-speed video camera with most of the remainder of the fluorescent light allowed to pass through the filter. The suspension is mixed by stirring before the experiment to avoid the separation of particles because of the gravity, and, thus, particles initially distribute uniformly in the container.

C. Film-flow approximation

To quantify the flow in a clear-fluid film, we propose a hypothetical continuum model of a stratified suspension at the limit $H \to 0$, where $H = \ell/h$ is the border resolution of the concentration interface [19,32] and indicates the ratio of the interparticle distance ℓ to the falling film thickness h for estimating the degree of the discreteness or the sharpness between the clear-fluid and particle-rich phases. To recall how to estimate the border resolution H, Fig. 3 schematically illustrates the bubble distributions for different H's. For sufficiently small H ($h > \ell$), stratification between the clear-fluid and particle-rich phases clearly occurs; thus, the swarm of particles is likely to exhibit a fluidlike behavior. Conversely, for sufficiently large H ($h < \ell$), a concentration interface does not clearly form; therefore, a particlelike behavior comes into being. We note that the index H indicates the sharpness of the concentration interface and is a dimensionless metric analogous to the Knudsen number Kn.

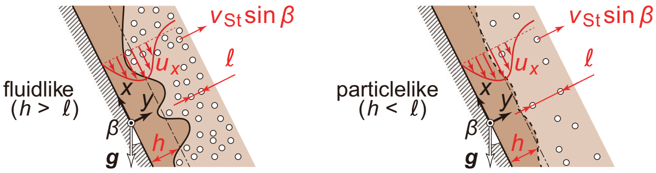

FIG. 3. Schematic of the relationship between clear-fluid layer thickness h and interparticle distance $\ell \approx a\langle\alpha\rangle^{-1/3}$ or $\approx [\pi a^3/(6\Delta z\langle\alpha\rangle)]^{1/2}$ for three-dimensional (experimental) or 2D (simulation) flow, respectively.

Here, we consider a thin liquid film confined to the wall vicinity ($h/L_y \ll 1$) in a rectangular container filled with a suspension of light particles and impose the acceleration of gravity $\boldsymbol{g}$ at a wall inclination of β as shown in Fig. 1(a). Based on the assumption that the stratified flow has a wall normal velocity u_y that is significantly smaller than its velocity along the wall u_x and follows a well-developed steady incompressible flow profile ($\partial u_x/\partial x = 0,\ \partial u_x/\partial t = 0,\ \boldsymbol{\nabla}\cdot\boldsymbol{u} = 0$), the parabolic velocity profile can be obtained as a solution to the Navier-Stokes equation as follows:

$$u_x(y) = \overline{u}_x(y) = -\frac{\langle\alpha\rangle\rho g\cos\beta}{2\mu}(2h-y)y, \tag{7}$$

where α is the particle concentration, ρ is the density of fluid, μ is the viscosity of fluid, $\overline{\cdots}$ denotes the time average, and $\langle\cdots\rangle$ denotes the volume average over the analytical domain, respectively. The maximum magnitude of velocity in the falling film $U_x (\equiv \max|\overline{u}_x|)$ at $y = h$ can then be obtained as

$$U_x = \frac{\langle\alpha\rangle\rho h^2 g\cos\beta}{2\mu}. \tag{8}$$

From a geometric approach, we assume the clear-fluid layer thickness, which is derived from the convective timescale $\tau(= L_x/U_x)$ and the wall normal velocity $v_{\rm St}\sin\beta$,

$$h \sim \tau v_{\rm St}\sin\beta, \tag{9}$$

where $v_{\rm St}[= \rho g a^2/(18\mu)]$ is the Stokes terminal velocity. From Eqs. (8) and (9), we obtain

$$U_x \sim \frac{\rho g}{2\mu}\left(\frac{\langle\alpha\rangle L_x^3 a^4\sin^2\beta\cos\beta}{81}\right)^{1/3}, \tag{10}$$

$$h \sim \left(\frac{L_x a^2\tan\beta}{9\langle\alpha\rangle}\right)^{1/3}. \tag{11}$$

In this paper, we consider the film flow on a smooth flat wall at a small film Reynolds number $< O(10)$ [12], and, thus, the shear induced turbulence is unlikely to result in the texture formation. The Froude number $\mathrm{Fr}[= 2U_x/(3\sqrt{\langle\alpha\rangle hg\cos\beta})]$ is a nondimensional parameter characterizing the importance of the inertial force relative to the force of gravity and serves as an indicator of the onset of the roll-wave instability [12]. The fluid motion of a falling liquid film in an inclined open channel can be described in terms of the magnitude of Fr as the flow becomes unstable beyond the theoretically estimated critical Froude number $\mathrm{Fr_c} = 2$ [15]. Using Eqs. (10) and (11), the Froude number and the border resolution of the concentration interface of the film-flow model can be hypothetically estimated as follows:

$$\mathrm{Fr_m} = \frac{\rho a}{9\mu}(L_x g\cos\beta)^{1/2}, \tag{12}$$

$$H_{\rm m} = \left(\frac{9a}{L_x\tan\beta}\right)^{1/3}. \tag{13}$$

We compare the fluid motion obtained from the roll wave in an open channel, simulation, experiment, and proposed

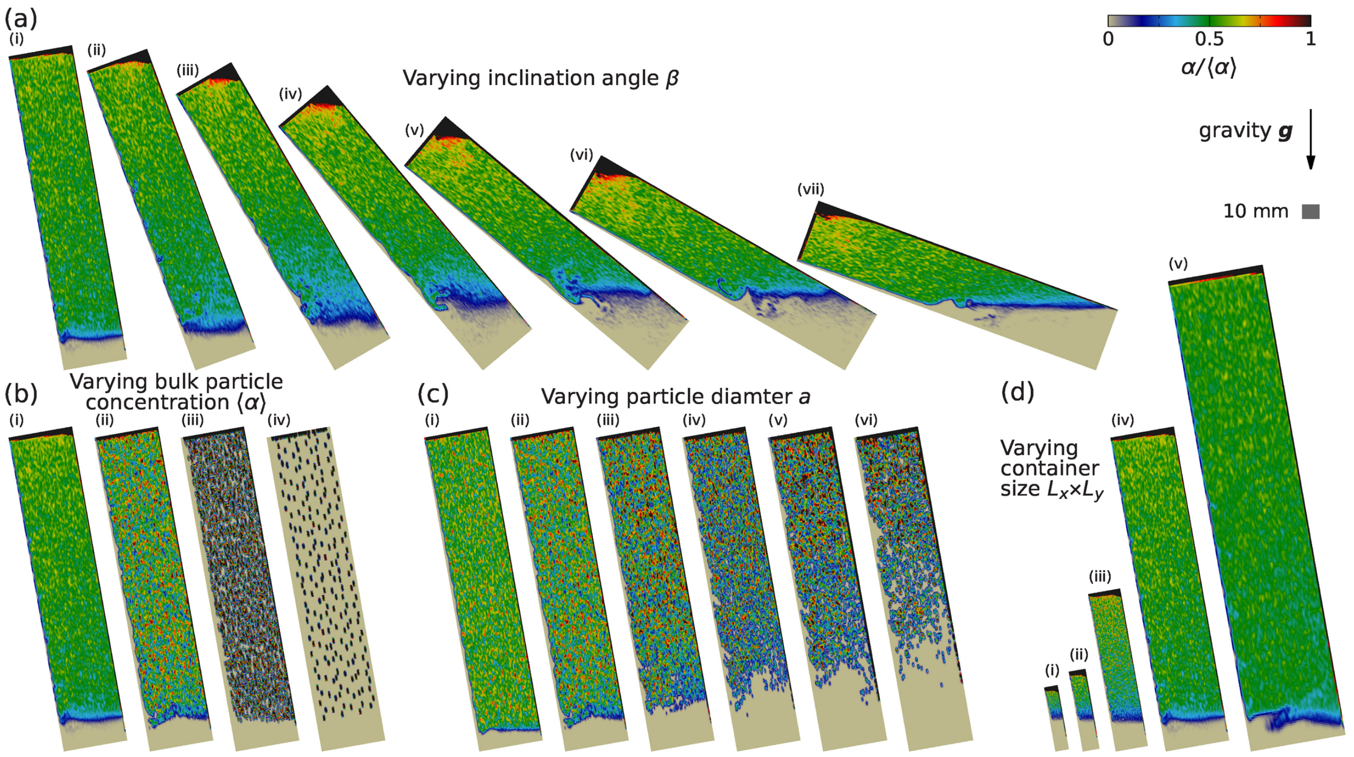

FIG. 4. Particle distribution under different conditions: (a) Varying inclination angle β, (b) varying bulk particle concentration $\langle\alpha\rangle$, (c) varying particle diameter a, and (d) varying container size $L_x \times L_y$. In each panel, one property is varied whereas the others are kept constant. In (a), $L_x \times L_y = 200$ mm $\times$ 40 mm, $a = 50 \pm 2$ μm, $\langle\alpha\rangle = 2 \times 10^{-2}$ are held constant whereas β varies: (a–i), $\beta = 10^\circ$; (a-ii), $\beta = 20^\circ$; (a-iii), $\beta = 30^\circ$; (a-iv), $\beta = 40^\circ$; (a-v), $\beta = 50^\circ$; (a-vi), $\beta = 60^\circ$; (a-vii), $\beta = 70^\circ$. In (b), $L_x \times L_y = 200$ mm $\times$ 40 mm, $a = 50 \pm 2$ μm, and $\beta = 10^\circ$ are held constant whereas $\langle\alpha\rangle$ varies: (b-i), $\langle\alpha\rangle = 2 \times 10^{-2}$; (b-ii), $\langle\alpha\rangle = 2 \times 10^{-3}$; (b-iii), $\langle\alpha\rangle = 2 \times 10^{-4}$; (b-iv), $\langle\alpha\rangle = 2 \times 10^{-5}$. In (c), $L_x \times L_y = 200$ mm $\times$ 40 mm, $\langle\alpha\rangle = 2 \times 10^{-2}$, $\beta = 10^\circ$ are held constant whereas a varies: (c-i), $a = 40 \pm 2$ μm; (c-ii), $a = 50 \pm 2$ μm; (c-iii), $a = 60 \pm 2$ μm; (c-iv), $a = 70 \pm 3$ μm; (c-v), $a = 80 \pm 3$ μm; (c-vi), $a = 90 \pm 3$ μm. In (d), $a = 50 \pm 2$ μm, $\langle\alpha\rangle = 2 \times 10^{-2}$, $\beta = 10^\circ$ are held constant whereas $L_x \times L_y$ varies: (d-i), $L_x \times L_y = 40 \times 8$ mm^2; (d-ii), $L_x \times L_y = 50 \times 10$ mm^2; (d-iii), $L_x \times L_y = 100 \times 20$ mm^2; (d-iv), $L_x \times L_y = 200 \times 40$ m^2; (d-v), $L_x \times L_y = 300 \times 60$ mm^2. A movie of a bubble swarm motion is available in the Supplemental Material [13].

mathematical model with continuum approximation. Thereby, we can extensively explore how the sharpness of the concentration interface affects the texture formation.

III. RESULTS AND DISCUSSION

A. Dynamic behavior of particle distribution

We start by showing that the simulated film thickness and wavelength of the particle-free fluid blobs are comparable to those obtained experimentally from the visualization of Guinness beer bubbles, indicating that these 2D simulations are as yet the most successful computational experiments of the cascading flow in Guinness beer. The unsteady motion of clear-fluid film is not limited to the conditions in Fig. 1 but persists across different inclination angles β, bulk particle concentrations $\langle\alpha\rangle$, particle diameters a, and container sizes $L_x \times L_y$ (see Fig. 4). Through these simulations, we use the same grid resolution and the same 3×3 points smoothed δ function. In Fig. 4, we can observe the following: the fluid motion becomes unsteady at small β, whereas it is stable at large β [Fig. 4(a)]; the particles behave collectively at large $\langle\alpha\rangle$ or at small a, whereas they behave individually at small $\langle\alpha\rangle$ or at large a [in Figs. 4(b) or 4(c)]; the fluid motion weakly depends on the container size $L_x \times L_y$ [Fig. 4(d)]. The formation and motion of the clear fluid can be observed in the corresponding high resolution movie (see the Supplemental Material [13]). The clear-fluid film forms in an inclined position owing to the Boycott effect, and for this reason, simulations with a standing ($\beta = 0$) or lying ($\beta = 90^\circ$) wall are unable to produce stratified convection (see also the Supplemental Material [13] for a video).

Next, we show the maximum magnitude of time-averaged downward velocity U_x [Fig. 5(a)] and clear-fluid layer thickness h [Fig. 5(b)] for various bulk particle concentrations and comparing the outputs obtained from the continuum model and simulation. It should be noted that, as the spatial distribution of the particle is discrete, there is no sharp interface between the clear and particle-rich fluids when the particle concentration is sufficiently small, no clear concentration interface forms. Following a previous theoretical study on particle sedimentation [33], h is defined as the distance from the wall at which the velocity of the falling liquid is the maximum. We also define a concentration-based thickness h_α and confirm that h and h_α are highly correlated (details are in Appendix A), which enables us to regard the velocity-based film thickness as a natural parameter for characterizing the flow. Figure 5(a) shows that the maximum magnitude of the simulated time-averaged velocities U_x and the rms

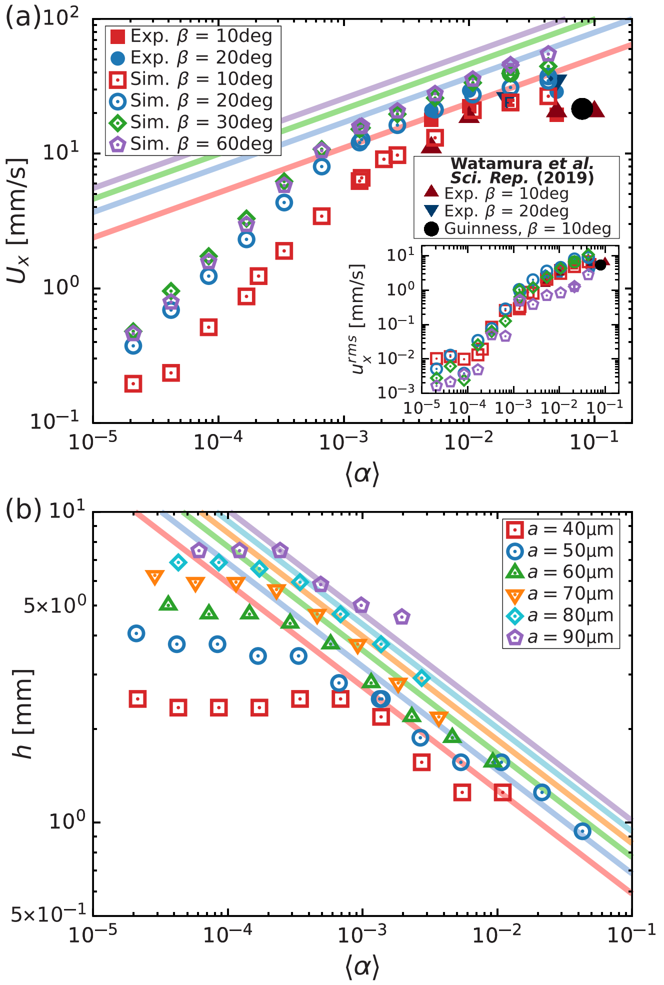

FIG. 5. (a) The maximum magnitudes of time-averaged velocity along the longitudinal wall U_x for various bulk particle concentrations $\langle\alpha\rangle$ and inclination angles β with the parameters $L_x \times L_y = 200 \times 40\ \text{mm}^2$ and $a = 50 \pm 2\ \mu\text{m}$ held constant. The lines indicate values of U_x obtained from Eq. (10); the inset plots the rms velocity u_x^{rms} against $\langle\alpha\rangle$. (b) Film thicknesses h for various values of $\langle\alpha\rangle$ and particle diameters a with $L_x \times L_y = 200 \times 40\ \text{mm}^2$ and $\beta = 30^\circ$ held constant. The lines indicate values of h calculated using Eq. (11).

value of the fluctuation component u_x^{rms} are consistent with the corresponding experimental values obtained using particle image velocimetry. The scaling exponents obtained from the simulation are also found to be closely correlated with those corresponding to the continuum model for $\langle\alpha\rangle > O(10^{-3})$ at which the continuum approximation holds ($H < 1$). We can also observe this scaling behavior in experiments as shown in Fig. 5(b) and in our preliminary study [19]. The magnitude relationships of film velocity or thickness with respect to inclination angle or particle diameter of the present continuum model are also found to be in qualitative agreement with the simulation, indicating that the proposed model explains the relationship over a wide range of inclination angles and particle diameters at $\langle\alpha\rangle > O(10^{-3})$.

To further validate the model, we compare the texture formations of Guinness beer in three glasses [Fig. 6(a)]. Although the bubble texture appears in the pint and shot glasses, the bubble motion in the cocktail glass produces a stable phase separation into a liquid and a head of foam. In Fig. 6(b), we map out a phase diagram of texture formation in L_x-β space with $\langle\alpha\rangle = 2 \times 10^{-2}$ and $a = 50 \pm 2\ \mu\text{m}$ derived from the scaled velocity fluctuation in the film flow. We measure the velocity at the fixed point h, and, thus, it is obvious that the texture formation, i.e., the spatiotemporal variation of clear-fluid layer thickness, is reflected in the velocity fluctuation [22]. Here, we visually and empirically define that the flow becomes unstable at $u_x^{\text{rms}}/U_x > 0.1$ because the velocity profile includes measurement errors or uncertainties and disturbance around a particle [12,19]. In Fig. 6(a), the flow is stable at large inclination angles and small container sizes and is unstable at small inclination angles and large container sizes. These stability conditions are fully consistent with our experimental

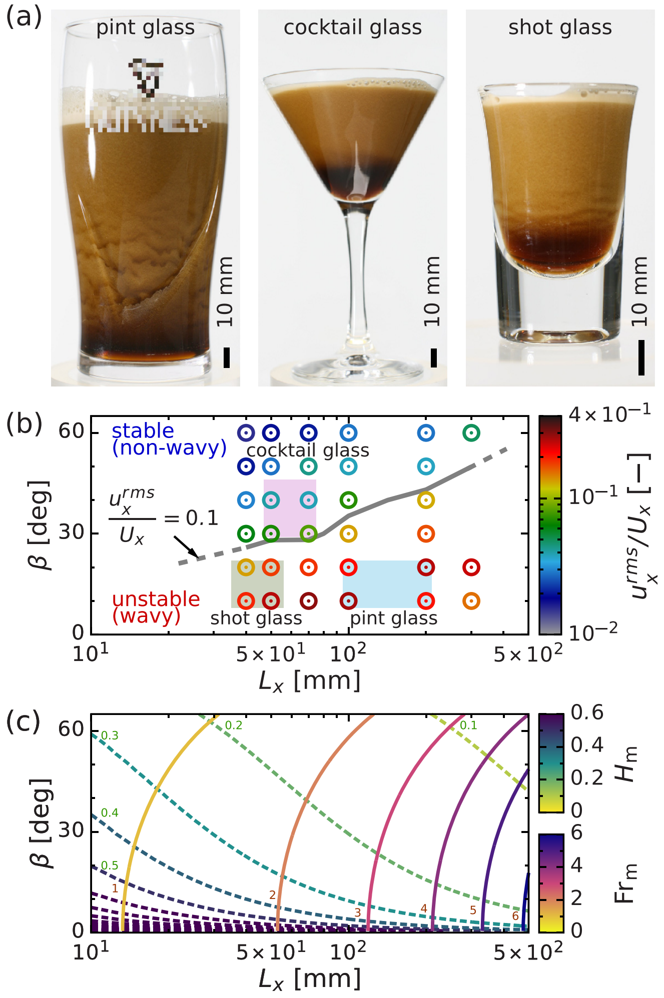

FIG. 6. (a) Snapshots of a bubble-concentration wave forming in: a pint glass (left), a cocktail glass (center), and a 1-oz (30-ml) shot glass (right). (b) Phase diagrams of scaled velocity fluctuation u_x^{rms}/U_x on the L_x-β plane. Circle color indicates the magnitude of the scaled velocity fluctuation u_x^{rms}/U_x; the gray line corresponds to the contour $u_x^{\text{rms}}/U_x = 0.1$ and serves as a visual guide indicating where instability begins. The shaded areas correspond to the typical dimensions of the glasses. (c) Contour plot of the Froude number Fr_m (solid line) and the border resolution of the concentration interface H_m (dotted line) on the L_x-β plane.

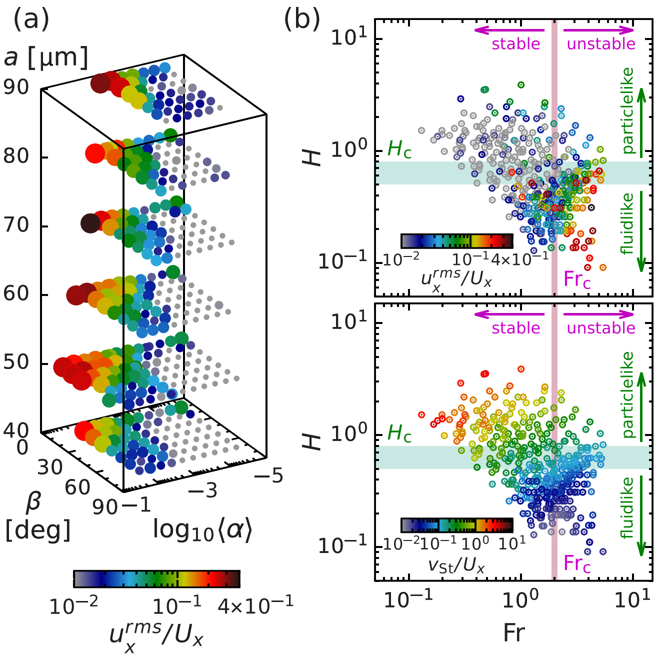

FIG. 7. Flow stability diagram. (a) Scaled velocity fluctuation u_x^{rms}/U_x for various bulk particle concentrations $\langle\alpha\rangle$, inclination angles β, and particle diameters a, where the color and size of the symbols indicate the magnitude of the scaled velocity fluctuation. (b) Scatter plots on the Fr-H plane of scaled velocity fluctuation u_x^{rms}/U_x (upper) and scaled Stokes' velocity v_{St}/U_x (lower). The vertical line indicates the critical Froude number for the onset of the instability Fr_{c}. The shaded area spans the range of the critical border resolution of the concentration interface of the particlelike or fluidlike-motion of suspension H_{c}.

observations on texture formation. At large L_x and small inclination angle β, the scaled velocity fluctuation u_x^{rms}/U_x exhibits significantly large value [Fig. 6(b)] and the modeled Froude number Fr_{m} exhibits a large value [Fig. 6(c)]. We can find this tendency as u_x^{rms}/U_x qualitatively correlates with Fr_{m}, even though there are clearly some discrepancies that are not accounted for by our oversimplification in continuum modeling in terms of, e.g., spatial development, hysteresis as Fr decreases over time, or volume exchange induced by rising particles.

B. Critical condition of the flow state

We then conducted a parametric study of massless Lagrangian tracking simulation in which the bulk particle concentration is varied from $O(10^{-5})$ to $O(10^{-2})$, the inclination angle β is varied from 10° to 70°, and the particle diameter a is varied from 40 to 90 μm, to gain a better understanding of the discrepancies between the results of the proposed model and the simulation for $\langle\alpha\rangle < O(10^{-3})$. The scaled velocity fluctuations over 380 cases are mapped out in Fig. 7(a). The results of this parametric study qualitatively confirm that the film flow becomes unstable at large $\langle\alpha\rangle$ and small β but with a dependence on a. Furthermore, u_x^{rms}/U_x is found to have a significantly large magnitude at small $\langle\alpha\rangle$ and small β; at these parameter settings, the individual particle motion relative to the fluid motion produces an extra disturbance around the particles that rapidly decays with the distance from the particle locations and is reflected in the velocity fluctuation.

To explain the fluid motion in terms of dimensionless numbers, i.e., using the terms of *hydrodynamics*, here we replot the scaled velocity fluctuation u_x^{rms}/U_x and particle velocity relative to the fluid velocity v_{St}/U_x in the Fr-H parameter space in Fig. 7(b). For $\mathrm{Fr} > \mathrm{Fr}_{\mathrm{c}}$ and $H < H_{\mathrm{c}}$, the flow becomes unstable, i.e., u_x^{rms}/U_x exhibits sufficiently large values because the roll wave is likely to be superimposed onto the fluidlike motion of the clear fluid. Note that we use the empirically obtained critical border resolution of the concentration interface H_{c} ranging from 0.5 to 0.8 [19]. For $\mathrm{Fr} > \mathrm{Fr}_{\mathrm{c}}$ and $H > H_{\mathrm{c}}$, by contrast, u_x^{rms}/U_x rapidly decreases because no clear concentration interface forms, and, therefore, the roll-wave instability no longer occurs. In this region, the particle stratification is unclear due to the particlelike situation and, thus, affects the onset of the roll-wave instability. Although the film flow is stable for $\mathrm{Fr} < \mathrm{Fr}_{\mathrm{c}}$, u_x^{rms}/U_x increases at large H because the individual particle velocity v_{St} becomes comparable to the film velocity U_x. This quadrant analysis successfully accounts for the critical condition of the continuum approximation, which is analogous to the continuum description of rarefied gas dynamics [1,2] and the roll-wave instability, despite the imperfections of the applied hypothesis.

C. Bubble cascade in carbonated water

The criterion of fluidlike and particlelike behaviors of the particle or bubble system explains why the cascading motion of bubbles has not been observed in drinks other than stout beers, such as Guinness beer. The formation of the bubble cascade in carbonated water which contains bubbles with diameters of 850 μm at a volume fraction of 4.5% (see Table I and Appendix B) and the unstable thin bubble-free films (satisfying $H < 0.5$, $h/L_y \ll 1$, and $v_{\mathrm{St}}/U_x \ll 1$) would require pouring the drink into a container with the wall inclined at an angle of $\sim 20^\circ$, a diameter of ~ 0.5 m, and height of ~ 1 m, corresponding to the approximate dimensions of a 200-l steel drum container (see Appendix C and Fig. 9). This also suggests that the bubbles in a beer fermentation vessel can flow collectively in the vicinity of an inclined wall; the related fluid motion is a key consideration in controlling the flow and heat and mass transfer to assure product quality in the brewing process. A further understanding of the fluidlike behavior of dispersed bodies will eventually uncover the dynamics of magma or lava flows [11], enabling us to gain a deeper insight into geological and volcanic island formations.

IV. CONCLUSION

In this paper, the collective motion of a bubble swarm in Guinness beer was studied by using a Lagrangian particle simulation and by developing the framework of a mathematical continuum model of stratified film flow in suspension. In the simulations with increasing the bulk particle concentration, the falling film velocity increases, and the film thickness decreases; this tendency is closely correlated with the continuum model at large particle concentrations, whereas at small particle concentrations, particles behave individually.

TABLE I. Physical quantities of bubbles produced in different drinks [mean ± standard deviation (SD), *n*].

	Bubble volume concentration α	Bubble mean diameter a (μm)	Interbubble distance ℓ (mm)
Guinness beer	$(9.2 \pm 0.7) \times 10^{-2}$, 30	59 ± 15, 301	0.13
Heineken beer	$(1.0 \pm 0.4) \times 10^{-2}$, 30	459 ± 31, 220	2.1
Champagne	$(8.5 \pm 0.6) \times 10^{-2}$, 30	422 ± 51, 252	0.95
Coke	$(2.3 \pm 0.4) \times 10^{-2}$, 30	469 ± 51, 213	1.6
Carbonated water	$(4.5 \pm 0.6) \times 10^{-2}$, 30	844 ± 111, 221	2.4

We found that the individual or collective motion of particles is scaled by the border resolution of concentration interface, which is analogous to the rarefied gas dynamics. The proposed model also predicts the critical condition of continuum approximation and the onset of the roll-wave instability without requiring experiments or simulations and suggests the general condition for the cascading bubble motion. We hope that our paper will motivate experiments or simulations on the motion of millimeter-sized bubbles in a large container to validate our model.

ACKNOWLEDGMENTS

This research was partially supported by JSPS KAKENHI Grants No. 18K13686 and No. 21H01248. Part of the simulation was performed on a supercomputing system HOKUSAI Great Wave and Big Waterfall at the Information Systems Division, RIKEN.

APPENDIX A: DEFINITION OF CONCENTRATION LAYER INTERFACE

The concentration interface of a stratified suspension cannot be uniquely well defined. There is no sharply concentrated interface between the clear-fluid layer and the particle-rich bulk because the spatial distribution of the particles is discrete, i.e., no concentration interface forms clearly at sufficiently low particle concentrations. Furthermore, an artificial grid length scale for the volume average must be introduced in the simulation to define the local particle concentrations, corresponding to the locally averaged particle volume at each grid point. From our preliminary experimental study [12], we hypothesized that the clear-fluid region is characterized by high falling speeds. Thus, following the suggestion of a theoretical study on particle sedimentation in an inclined container [33], we chose the clear-fluid film thickness h—the distance from the wall at which the velocity of falling liquid is maximum—as a well-defined quantity to indicate thickness. We also define a concentration-based thickness h_α as the distance from the wall to the position at which half of the time-averaged particle concentration occurs, i.e., the position at which the time-averaged particle concentration is $\overline{\alpha}(h_\alpha) = 0.5\langle\alpha\rangle$. To determine whether the velocity-based thickness h could reasonably reflect the concentration-based thickness h_α, we compare the clear-fluid layer thicknesses in Fig. 8 and confirm that h and h_α are highly correlated—albeit with some differences—when the velocity fluctuation is relatively small ($u_x^{\mathrm{rms}}/U_x < 0.1$). Based on this, we propose that the velocity-based film thickness can be considered a natural choice to characterize the flow.

APPENDIX B: BUBBLE SIZE DISTRIBUTION

We measured the bubble diameters of each drink using image analysis. Within 10 s of decanting, we poured each drink into a trapezium glass with a height of 120 mm, a width of 60 mm, and bottom and top depths of 30 and 52 mm [12], respectively. Within 20 s of pouring, bubble images were captured over, at least, three experimental runs per drink using a high-speed video camera with a microscopic lens. Hollow spherical glass particle images were taken using a still-image camera with a microscopic lens. At least, 200 samples were measured per case. The bubble and particle size distributions are summarized in Table I along with the means, SDs, and corresponding sample size (n). A canned draught Guinness beer is a supersaturated solution of nitrogen gas which dissolves less than carbon dioxide gas [35], and for this reason, Guinness beer contains small-diameter bubbles which are only 1/10 the size of those in other drinks.

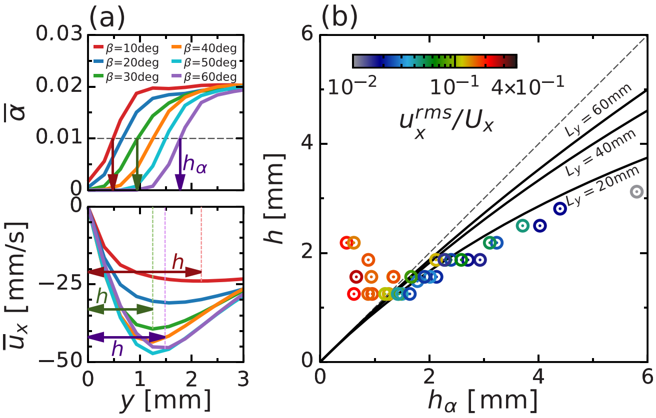

FIG. 8. Definition of clear-fluid thickness. (a) Temporal average of particle concentration (top) and liquid-phase velocity along the longitudinal wall (bottom) for various inclination angles β. (b) Comparison of concentration- and velocity-based clear-fluid layer thicknesses. The dashed line indicates $h = h_\alpha$; the solid line denotes $h = L_y h_\alpha/(L_y + 2h_\alpha)$ as obtained from a mathematical model including the upward flow [34].

APPENDIX C: CONTINUUM APPROXIMATION FOR MODERATE PARTICLE REYNOLDS NUMBERS

For moderate particle Reynolds number ranges of $2 < \mathrm{Re} < 500$, we use the empirical drag coefficient [36] given by

$$C_D = 10\,\mathrm{Re}^{-1/2}. \tag{C1}$$

Assuming a buoyant bubble motion in an infinite quiescent viscous liquid, the terminal velocity of a bubble can be obtained as follows:

$$v_\mathrm{t} = a\left(\frac{4\rho g}{225\mu}\right)^{1/3}. \tag{C2}$$

Then, using Eqs. (8), (9), and (C2), we can obtain the maximum velocity magnitude in the falling film U_x, the clear-fluid layer thickness h, the Froude number Fr, and the border resolution of the concentration interface H, respectively, as follows:

$$U_x \sim \left(\frac{2\rho^5\langle\alpha\rangle^3 L_x^6 a^6 g^7 \sin^6\beta\,\cos^3\beta}{15^4\mu^5}\right)^{1/9}, \tag{C3}$$

$$h \sim \left(\frac{2^5 L_x^3 a^3 \mu^2 \tan^3\beta}{15^2\rho^2\langle\alpha\rangle^3 g}\right)^{1/9}, \tag{C4}$$

$$\mathrm{Fr_m} \sim \left(\frac{2^5 L_x^3 \rho^4 g^2 \cos^3\beta}{3^8 5^2 \mu^4}\right)^{1/6}, \tag{C5}$$

$$H_\mathrm{m} \sim \left(\frac{15^2\rho^2 a^6 g}{2^5 L_x^3 \mu^2 \tan^3\beta}\right)^{1/9}. \tag{C6}$$

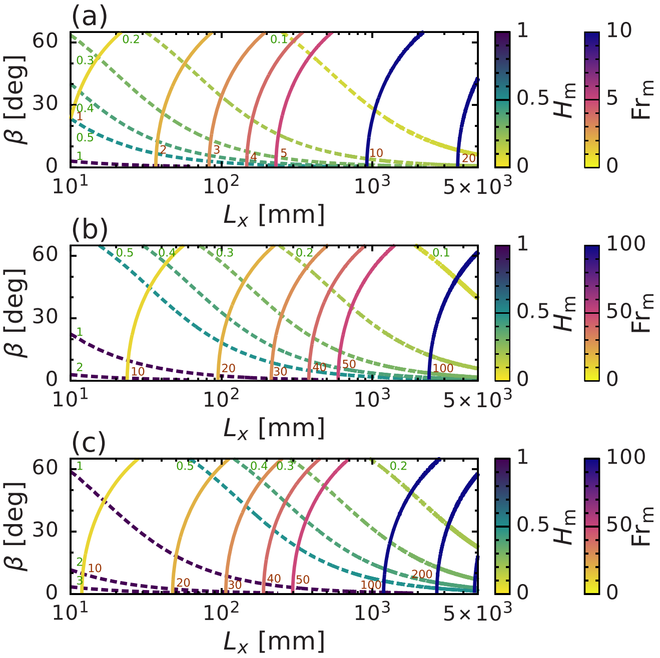

FIG. 9. Contour plot of the Froude number $\mathrm{Fr_m}$ (solid line) and the border resolution of the concentration interface H_m (dotted line) on the L_x-β plane; (a) $a = 60\ \mu$m corresponding to Guinness beer; (b) $a = 400\ \mu$m corresponding to Heineken beer, champagne, and Coke; (c) $a = 800\ \mu$m corresponding to carbonated water. The estimations are produced by the continuum model in Eqs. (12) and (13) at $a = 60\ \mu$m, whereas Eqs. (C5) and (C6) at $a = 400$ and $800\ \mu$m.

Figure 9 shows the stability diagram for various drinks containing bubbles where we use the bubble properties shown in Table I.

---

[1] G. A. Bird, *Molecular Gas Dynamics and the Direct Simulation of Gas Flows*, edited by J. M. Brady, C. E. Brennan, W. R. Eatock Taylor, M. Y. Hussaini, T. V. Jones, and J. van Bladel, Oxford Engineering Sciences Series (Clarendon, Oxford University Press, Oxford, 1994).

[2] J. Happel and H. Brenner, *Low Reynolds Number Hydrodynamics* (Martinus Nijhoff, The Hague, 1983).

[3] R. D. Maladen, Y. Ding, C. Li, and D. I. Goldman, Undulatory swimming in sand: Subsurface locomotion of the sandfish lizard, Science **325**, 314 (2009).

[4] A. Daerr and S. Douady, Two types of avalanche behaviour in granular media, Nature (London) **399**, 241 (1999).

[5] G. Félix and N. Thomas, Relation between dry granular flow regimes and morphology of deposits: formation of levées in pyroclastic deposits, Earth Planet. Sci. Lett. **221**, 197 (2004).

[6] A. Penn, T. Tsuji, D. O. Brunner, C. M. Boyce, K. P. Pruessmann, and C. R. Müller, Real-time probing of granular dynamics with magnetic resonance, Sci. Adv. **3**, e1701879 (2017).

[7] C. P. McLaren, T. M. Kovar, A. Penn, C. R. Müller, and C. M. Boyce, Gravitational instabilities in binary granular materials, Proc. Natl. Acad. Sci. USA **116**, 9263 (2019).

[8] M. S. Plesset and H. Winet, Bioconvection patterns in swimming microorganism cultures as an example of Rayleigh-Taylor instability, Nature (London) **248**, 441 (1974).

[9] P. Chakraborty, G. Gioia, and S. W. Kieffer, Volcanic mesocyclones, Nature (London) **458**, 497 (2009).

[10] S. Carey, Influence of convective sedimentation on the formation of widespread tephra fall layers in the deep sea, Geology **25**, 839 (1997).

[11] M. Manga, Waves of bubbles in basaltic magmas and lavas, J. Geophys. Res.: Solid Earth **101**, 17457 (1996).

[12] T. Watamura, F. Iwatsubo, K. Sugiyama, K. Yamamoto, Y. Yotsumoto, and T. Shiono, Bubble cascade in guinness beer is caused by gravity current instability, Sci. Rep. **9**, 5718 (2019).

[13] See Supplemental Material at http://link.aps.org/supplemental/10.1103/PhysRevE.103.063103 for videos of experimentally observed bubble motion in drinks and numerically simulated cascading motion of bubble swarm.

[14] A. Boycott, Sedimentation of blood corpuscles, Nature (London) **104**, 532 (1920).

[15] D. J. Needham and J. H. Merkin, On roll waves down an open inclined channel, Proc. R. Soc. London, Ser. A **394**, 259 (1984).

[16] N. E. Shafer and R. N. Zare, Through a beer glass darkly, Phys. Today **44**(10), 48 (1991).

[17] G. Liger-Belair, G. Polidori, and P. Jeandet, Recent advances in the science of champagne bubbles, Chem. Soc. Rev. **37**, 2490 (2008).

[18] S. Takagi and Y. Matsumoto, Surfactant effects on bubble motion and bubbly flows, Annu. Rev. Fluid Mech. **43**, 615 (2011).

[19] M. Koyama, T. Watamura, and K. Sugiyama, Simultaneous photobleaching molecular tagging velocimetry for density-stratified flows of suspensions, Exp. Fluids **60**, 148 (2019).

[20] M. Robinson, A. C. Fowler, A. Alexander, and S. B. O'Brien, Waves in guinness, Phys. Fluids **20**, 067101 (2008).

[21] E. Benilov, C. Cummins, and W. Lee, Why do bubbles in guinness sink? Am. J. Phys. **81**, 88 (2013).

[22] S. Kalliadasis, C. Ruyer-Quil, B. Scheid, and M. G. Velarde, *Falling Liquid Films*, Applied Mathematical Sciences Vol. 176 (Springer, London, 2011).

[23] I. M. Mazzitelli, D. Lohse, and F. Toschi, On the relevance of the lift force in bubbly turbulence, J. Fluid Mech. **488**, 283 (2003).

[24] P. A. Cundall and O. D. L. Strack, A discrete numerical model for granular assemblies, Géotechnique **29**, 47 (1979).

[25] Y. Tsuji, T. Kawaguchi, and T. Tanaka, Discrete particle simulation of two-dimensional fluidized bed, Powder Technol. **77**, 79 (1993).

[26] M. R. Maxey and J. J. Riley, Equation of motion for a small rigid sphere in a nonuniform flow, Phys. Fluids **26**, 883 (1983).

[27] X. Yang, X. Zhang, Z. Li, and G.-W. He, A smoothing technique for discrete delta functions with application to immersed boundary method in moving boundary simulations, J. Comput. Phys. **228**, 7821 (2009).

[28] J. J. Stickel and R. L. Powell, Fluid mechanics and rheology of dense suspensions, Annu. Rev. Fluid Mech. **37**, 129 (2005).

[29] R. H. Davis and A. Acrivos, Sedimentation of noncolloidal particles at low reynolds numbers, Annu. Rev. Fluid Mech. **17**, 91 (1985).

[30] R. J. Adrian, Particle-imaging techniques for experimental fluid mechanics, Annu. Rev. Fluid Mech. **23**, 261 (1991).

[31] R. Lindken and W. Merzkirch, A novel PIV technique for measurements in multiphase flows and its application to two-phase bubbly flows, Exp. Fluids **33**, 814 (2002).

[32] S. Harada, T. Mitsui, and K. Sato, Particle-like and fluid-like settling of a stratified suspension, Eur. Phys. J. E **35**, 1 (2012).

[33] A. Acrivos and E. Herbolzheimer, Enhanced sedimentation in settling tanks with inclined walls, J. Fluid Mech. **92**, 435 (1979).

[34] W. T. Lee, S. Kaar, and S. B. O'Brien, Sinking bubbles in stout beers, Am. J. Phys. **86**, 250 (2018).

[35] W. T. Lee, J. S. McKechnie, and M. G. Devereux, Bubble nucleation in stout beers, Phys. Rev. E **83**, 051609 (2011).

[36] H. S. Allen, XXXI. The motion of a sphere in a viscous fluid, The London, Edinburgh, and Dublin Philos. Mag. J. Sci. **50**, 323 (1900).